Submitted to ApJ Letters

Deeply Embedded Protostellar Population in the 20 km s^{-1} Cloud of the Central Molecular Zone

Xing Lu[1,2,3,4], Qizhou Zhang[2], Jens Kauffmann[5], Thushara Pillai[5], Steven N. Longmore[6], J. M. Diederik Kruijssen[7], Cara Battersby[2], and Qiusheng Gu[1,3,4]

[1] *School of Astronomy and Space Science, Nanjing University, Nanjing 210093, P. R. China;*

xinglv.nju@gmail.com

[2] *Harvard-Smithsonian Center for Astrophysics, 60 Garden Street, Cambridge, MA 02138, USA*

[3] *Key Laboratory of Modern Astronomy and Astrophysics, Nanjing University, Nanjing 210093, P. R. China*

[4] *Collaborative Innovation Center of Modern Astronomy and Space Exploration, Nanjing 210093, P. R. China*

[5] *Max Planck Institut für Radioastronomie, Auf dem Hügel 69, D-53121 Bonn, Germany*

[6] *Astrophysics Research Institute, Liverpool John Moores University, 146 Brownlow Hill, Liverpool L3 5RF, UK*

[7] *Zentrum für Astronomie der Universität Heidelberg, Astronomisches Rechen-Institut, Mönchhofstraße 12-14, 69120 Heidelberg, Germany*

ABSTRACT

We report the discovery of a population of deeply embedded protostellar candidates in the 20 km s^{-1} cloud, one of the massive molecular clouds in the Central Molecular Zone (CMZ) of the Milky Way, using interferometric submillimeter continuum and H_2O maser observations. The submillimeter continuum emission shows five 1-pc scale clumps, each of which further fragments into several 0.1-pc scale cores. We identify 17 dense cores, among which 12 are gravitationally bound. Among the 18 H_2O masers detected, 13 coincide with the cores and probably trace outflows emanating from the protostars. There are also 5 gravitationally bound dense cores without H_2O maser detection. In total the 13 masers and 5 cores may represent 18 protostars with spectral types later than B1 or potential growing more massive stars at earlier evolutionary stage, given the non-detection in the centimeter radio continuum. In combination with previous studies of CH_3OH masers, we conclude that the star formation in this cloud is at an early evolutionary phase, before the presence of any significant ionizing or heating

sources. Our findings indicate that star formation in this cloud may be triggered by a tidal compression as it approaches pericenter, similar to the case of G0.253+0.016 but with a higher star formation rate, and demonstrate that high angular resolution, high sensitivity maser and submillimeter observations are a promising technique to unveil deeply embedded star formation in the CMZ.

Subject headings: Galaxy: center — ISM: clouds — stars: formation

1. INTRODUCTION

The inner 500-pc region of the Galaxy, known as the Central Molecular Zone (CMZ), is rich in dense molecular gas, but the current star formation is unusually inactive. Other than the few star forming regions such as Sgr B2 (Goldsmith et al. 1990; Qin et al. 2008), Sgr A complex (Ekers et al. 1983; Yusef-Zadeh et al. 2010), and Sgr C (Kendrew et al. 2013), most CMZ clouds appear to be inactive in star formation (e.g., G0.253+0.016; Lis et al. 1994; Longmore et al. 2012; Kauffmann et al. 2013b; Johnston et al. 2014; Mills et al. 2015; Rathborne et al. 2015). This inactivity is in contrast to the general star formation relation that has been established for the Galactic disk clouds as well as external galaxies, which presents a good correlation between the amount of dense molecular gas and the star formation rate. The overall star formation rate in the CMZ is an order of magnitude lower than the prediction of this correlation (Longmore et al. 2013a).

Recent theoretical works by Kruijssen et al. (2014) and Krumholz & Kruijssen (2015) point out that star formation in the CMZ could be regulated by the strength of turbulence: the inflowing gas through the Galactic bar drives strong turbulence, resulting in episodes of low star formation activity; when the turbulence finally dissipates, a burst of star formation takes place. Such dissipation of the turbulence could be induced by compressive tides during a close passage to the bottom of the gravitational potential near Sgr A* (Longmore et al. 2013b). In the simulations of Kruijssen et al. (2015), the massive molecular clouds in the CMZ are found to be in several streams of open trajectory centered at Sgr A* with a radius of ∼100 pc. The 20 $\mathrm{km\,s^{-1}}$ cloud, a massive ($\gtrsim$1.6×10^5 $M_\odot$; Bally et al. 2010) molecular cloud named after its radial velocity, appears to be close to pericenter passage with Sgr A*, therefore could be in the process of turbulence dissipation. In this scenario, we expect to observe increasing dense gas fraction and signs of early star formation in the 20 $\mathrm{km\,s^{-1}}$ cloud.

Previous interferometric observations have found one H II region (Downes et al. 1979), and several H_2O masers (Sjouwerman et al. 2002; Caswell et al. 2011) in this cloud. However, the maser observations were sensitivity-limited (usually $\gtrsim$30 $\mathrm{mJy\,beam^{-1}}$ per 0.2 $\mathrm{km\,s^{-1}}$ channel), hence could miss faint sources that trace star formation of lower masses or at early evolutionary stages. Here we use interferometric submillimeter observations to trace dense cores, and interferometric H_2O maser observations with a sensitivity of ∼5 times higher than previous studies to trace embedded protostars. Throughout the paper, we adopt a distance to the Galactic Center of 8.4 kpc (Reid

et al. 2009).

2. OBSERVATIONS AND DATA REDUCTION

2.1. SMA Observations

In 2013, we observed a mosaic of eight positions in the 20 $\mathrm{km\,s^{-1}}$ cloud with the Submillimeter Array[8] (SMA) in its compact and sub-compact configurations at 230 GHz band. The primary beam size is $\sim$56″. All observations share the same correlator setup: the rest frequencies of 216.9–220.9 GHz are covered in one sideband, and 228.9–232.9 GHz are covered in the other sideband, with a uniform channel width of 0.812 MHz, equivalent to 1.1 $\mathrm{km\,s^{-1}}$ at 230 GHz. Observation details are listed in Table 1.

The visibility data were calibrated using MIR[9] and inspected and imaged using MIRIAD (Sault et al. 1995) and CASA (McMullin et al. 2007). Continuum was extracted from line free channels and imaged using data from both sidebands. Spectral lines were split from the continuum-subtracted visibility data and were imaged separately. We used a robust parameter of 0.5 when CLEANing images. The resulting continuum image has a clean beam of 4.9″×2.8″ (equivalent to 0.20 pc×0.11 pc) with a position angle of 5.2° and an rms of 3 $\mathrm{mJy\,beam^{-1}}$. Typical rms of spectral lines images is $\sim$0.13 $\mathrm{Jy\,beam^{-1}}$ per 1.1 $\mathrm{km\,s^{-1}}$ channel.

2.2. VLA Observations

In 2013 May, we observed a mosaic of three positions in this cloud with the National Radio Astronomy Observatory (NRAO)[10] Karl G. Jansky Very Large Array (VLA) in the DnC configuration at K band, with a primary beam size of $\sim$2′. The WIDAR correlator was configured to cover the H_2O maser at 22.2 GHz using a 16 MHz subband in dual polarizations, as well as 1.3 cm continuum using eight 128 MHz subbands in full polarizations. For the H_2O maser, the subband was split into 1024 channels with a channel width of 15.6 kHz, equivalent to 0.2 $\mathrm{km\,s^{-1}}$. Observation details are listed in Table 1.

The visibility data were calibrated and imaged using CASA. Continuum was extracted from line free channels of the 128 MHz subbands, leading to a total bandwidth of 0.9 GHz. The robust parameter we used in CLEAN is 0.5. For the H_2O maser image, the resulting clean beam is

[8]The Submillimeter Array is a joint project between the Smithsonian Astrophysical Observatory and the Academia Sinica Institute of Astronomy and Astrophysics and is funded by the Smithsonian Institution and the Academia Sinina.

[9]https://www.cfa.harvard.edu/~cqi/mircook.html

[10]The National Radio Astronomy Observatory is a facility of the National Science Foundation operated under cooperative agreement by Associated Universities, Inc.

$3.5'' \times 2.4''$ (equivalent to 0.14 pc×0.10 pc) with a position angle of 5.7°. The rms in each 0.2 km s^{-1} channel is 6 mJy beam^{-1}, but can be significantly larger in channels where signals are dynamic range limited.

3. RESULTS

3.1. SMA Dense Cores

The SMA 1.3 mm continuum emission revealed five clumps of 1-pc scales in the 20 km s^{-1} cloud, labelled as C1–C5 in Figure 1. In the projected plane of the sky they are equally spaced by ∼1 pc and aligned along the densest part of the cloud. All the clumps appear to have substructures, or cores, among which C4 is the most prominent one which presents at least 6 cores.

After a visual inspection of dust peaks with fluxes above 5σ levels, we identified 17 cores. Then we fitted 2D Gaussians to obtain their positions, deconvolved sizes, and primary-beam corrected continuum fluxes. We assumed a gas-to-dust mass ratio of 100, a dust emissivity index $\beta = 1.5$, and applied the dust temperature $T_{\rm dust} = 19$ K (see Figure 1) and a mean continuum frequency of 225 GHz, then the core masses were calculated following Beuther et al. (2005). The results are listed in Table 2.

3.2. VLA H_2O Masers

The VLA observations revealed 18 H_2O masers in this cloud, marked by crosses and labeled as W1–W18 in Figure 2. 15 out of 18 are within the SMA field, among which 13 spatially coincide with dust emission peaks above 5σ levels. The velocities of these 13 masers are all within ±20 km s^{-1} with respect to the core velocities. Properties of these H_2O masers are summarized in Table 3 and their spectra are shown in Figure 2.

Among the previous H_2O maser surveys toward the CMZ, Walsh et al. (2011) did not find any masers in this cloud using the Mopra telescope at a sensitivity of 1–2 Jy, while Caswell et al. (2011) detected three masers, using ATCA at a sensitivity of $\lesssim$0.1 Jy: two of them are consistent with W13 and W15, respectively, within a position uncertainty of $2''$; the other one is in C1, offset from the masers we detected by $\sim 3''$. In addition, Sjouwerman et al. (2002) serendipitously detected 10 H_2O masers in this cloud while studying OH/IR stars, all of which they concluded to be connected to star formation given the non-detection of OH/IR stars. One of them is consistent with W5, while the other 9 are scattered in C4: one is offset from any masers we detected, 8 are likely consistent with W10, W11–W13, and W15.

4. DISCUSSIONS

4.1. The Gravitational Equilibrium of the Dense Cores

We analyze the virial status of the cores. The virial parameter is defined as $\alpha = 5\sigma_v^2 R/(GM_{\rm core})$ (Bertoldi & McKee 1992; Kauffmann et al. 2013a), where $\sigma_v = {\rm FWHM}/\sqrt{8\ln 2}$ is the one-dimensional velocity dispersion. For a self-gravitating, non-magnetized core, the critical virial parameter is 2, above which the core is unbound and may expand, while below which it is bound and may collapse.

The N_2H^+ line has a critical density of $\gtrsim 10^6$ cm^{-3}, and is superior for tracing dense gas than the spectral lines in our SMA data such as $C^{18}O$ or H_2CO. To derive line widths of the cores, we obtain the SMA N_2H^+ 3–2 data (Kauffmann et al. in prep.), then fit Gaussians to the mean N_2H^+ spectra of the cores. For the 4 cores without N_2H^+ detections, we fit their mean $C^{18}O$ or H_2CO spectra instead. Two cores, C3-P2 and C3-P3, do not present any of the three dense gas tracers, thus are excluded in the analysis. The results are listed in Table 2.

Among the 15 cores included in the analysis, 12 have $\alpha < 2$. The two most massive cores, C1-P1 and C4-P1, have virial parameters as low as ∼0.2. Three cores have $\alpha > 2$, including C4-P4 which associates with an H_2O maser.

The masses themselves have large uncertainties: the errors in the core masses are a factor of 1.2–1.8, while the virial masses are sensitive to the selection of line widths and the errors are a factor of 1.7–2, according to the simulations of Battersby et al. (2010) that take errors in all variables of the mass estimates into account. Besides, the magnetic field might be dynamically important on pc scales in the CMZ clouds, as suggested by the ordered magnetic vectors in G0.253+0.016 (Pillai et al. 2015) which derive a magnetic flux density of ∼5 mG from the Chandrasekhar-Fermi method. Within these uncertainties, the 12 cores with $\alpha < 2$ are gravitationally bound.

4.2. The Nature of the H_2O Masers

H_2O masers in star-forming regions are usually excited in shocked ambient gas (Elitzur et al. 1989), therefore are used to trace protostellar outflows. However, they can also be excited in the envelope of evolved stars (Sjouwerman & van Langevelde 1996) or excited by shocks created in large-scale dynamic processes (e.g., cloud collisions, Tarter & Welch 1986). We need to exclude these scenarios before using the H_2O masers as star formation indicators.

First, we compare the coordinates and velocities of the H_2O masers with the evolved star catalogues in Lindqvist et al. (1992), Sevenster et al. (1997), and Sjouwerman et al. (1998, 2002) which used OH or SiO masers as tracers. Two H_2O masers (W6, W18) are consistent with evolved stars (red crosses in Figure 2). The other 16 H_2O masers do not have known evolved star counterparts.

Second, we compare with the class I CH_3OH masers in Yusef-Zadeh et al. (2013), which are collisionally pumped and trace large-scale dynamics. None of the H_2O masers spatially coincide

with the class I CH_3OH masers. Most of the H_2O masers coincide with the dense cores, instead of uniformly scatter like the class I CH_3OH masers. Their velocities are usually offset by ± 20 km s^{-1} from the core velocities, which is easily seen in masers tracing outflows, instead of all showing the same value at the presumable shock interaction velocity. All these facts suggest that the H_2O masers are unlikely connected to large-scale shocks.

Therefore, the 16 H_2O masers without evolved star counterparts, in particular, the 13 masers coincident with the dense cores, are likely associated with outflows. Indeed, we find signatures of outflows associated with these cores traced by SiO, SO, and HNCO lines in the SMA images, which we will present in a forthcoming paper. A correlation between luminosities of H_2O masers and protostars (e.g., Palla et al. 1993) suggests that the more luminous masers ($\gtrsim 10^{-6}$ $L_\odot$, see Table 3) may correspond to early B-type stars of $\gtrsim 10^3$ $L_\odot$, while the characteristic luminosity of $\sim 10^{-7}$ $L_\odot$ for most masers is usually found in low- or intermediate-mass protostars (e.g., Furuya et al. 2001).

4.3. Comparison with Other Star Formation Tracers

The free-free emission from H II regions is a reliable star formation tracer. However, only one H II region has been found in this cloud (Downes et al. 1979), which is verified by our VLA 1.3 cm continuum observation (Figure 1). Assuming an electron temperature of 10^4 K, with a continuum flux of 0.12 Jy, its ionizing photon rate is 9×10^{47} s^{-1} (Mezger & Henderson 1967), corresponding to an O9 star of 19 $M_\odot$ (Mottram et al. 2011). The non-detection of any other H II regions at a sensitivity of 100 μJy may suggest no protostars earlier than B1 above $\sim$10 $M_\odot$, or simply an early evolutionary phase without any visible ionizing sources.

Yusef-Zadeh et al. (2009) identified YSOs in the CMZ using the *Spizter* 8 μm and 24 μm emission, and found three in the vicinity of this cloud, but none of them are within the cloud itself. The only visible infrared point source within the cloud in the *Spitzer* mid-infrared images is the H II region. Therefore, the deeply embedded protostars are not observable in the infrared bands, probably due to the large column density ($\gtrsim 10^{23}$ cm^{-2}) which obscures the embedded sources.

CH_3OH masers have been found in star-forming regions in the Galactic disk, and are classified as class I or class II, depending on whether they are collisionally or radiatively pumped (Menten 1991; Fontani et al. 2010). Recent class I CH_3OH maser observations toward the CMZ (Yusef-Zadeh et al. 2013; Mills et al. 2015) suggested that these masers may not trace star formation, but may have cosmic ray or cloud-scale dynamic origins. On the other hand, radiatively pumped class II CH_3OH masers have been reliable tracers of high-mass star formation (Urquhart et al. 2015). The methanol multi-beam survey (MMB, Caswell et al. 2010) did not detect any class II (6.7 GHz) CH_3OH masers at a sensitivity of 0.17 Jy in this cloud. By contrast, four H_2O masers in our results (W3, W5, W11, W15) are detectable at 3σ levels with the same sensitivity.

4.4. Implications for Star Formation in the 20 km s^{-1} Cloud

As discussed above, we find 13 H_2O masers associated with the dense cores and probably trace protostellar outflows, and 5 dense cores without H_2O maser detection but gravitationally bound. In total, they may represent 18 protostellar candidates. This number should be a lower limit because the dense cores could harbor multiple protostars. By contrast, previous observations found ∼10 H_2O masers most of which are concentrated in C4, corresponding to 6 protostellar candidates in our sample. In the following we discuss the implication of our results for the evolutionary phase and star formation activity of the 20 km s^{-1} cloud.

The evolutionary phases of star formation traced by H_2O masers is under debate (e.g., Szymczak et al. 2005; Breen et al. 2010). Recent follow-up studies of the unbiased MMB survey suggest that while not as well-defined as the other masers, H_2O masers in general trace the protostellar phase when outflows emerge (Breen et al. 2014; Titmarsh et al. 2014). On the other hand, these studies seem to converge to the conclusion that class II CH_3OH masers trace a well-defined evolutionary phase (e.g., after protostars start to heat ambient gas and before the UC H II region phase). For the 20 km s^{-1} cloud, the large population of H_2O masers and the virtually non-detection of class II CH_3OH masers so far, combining with the non-detection of any prominent UC H II regions, are likely indicative of two alternative scenarios: an early evolutionary phase when high-mass protostars have not started to heat or ionize the ambient gas, but have developed outflows, similar to the situation in infrared dark clouds (IRDCs); or a cluster of low- or intermediate-mass protostars, whose outflows power the H_2O masers but whose radiation is not enough to create class II CH_3OH masers or visible H II regions. The former may be preferable because the more luminous masers may trace high-mass protostars (see Section 4.2).

No matter which scenario it is, the 18 protostellar candidates traced by H_2O masers and gravitationally bound cores suggest more active star formation than that traced by free-free or infrared emission (one H II region). Sensitive maser and submillimeter observations could be a promising method to trace incipient star formation in other massive clouds in the CMZ.

In the orbital models of Kruijssen et al. (2015), G0.253+0.016 is also close to pericenter passage with Sgr A*, but in a different gas stream. G0.253+0.016 has a similar mass as the 20 km s^{-1} cloud (∼1.3×10^5 $M_\odot$; Longmore et al. 2012), but only has one known H_2O maser (Lis et al. 1994) and one gravitationally bound dense core associated with the maser (Kauffmann et al. 2013b; Rathborne et al. 2015). The progression of star formation activity from G0.253+0.016 to Sgr B2 supports the tidal compression and triggered collapse model proposed by Longmore et al. (2013b). The 20 km s^{-1} cloud could be a second case of such triggering. Based on the number of masers and the amount of dense gas contained in cores, the current star formation rate in the 20 km s^{-1} cloud is likely higher than in G0.253+0.016. The difference might be due to variations in the local environment in the streams.

5. CONCLUSIONS

We have found 18 protostellar candidates traced by dust emission and H_2O masers in the 20 $km\,s^{-1}$ cloud, most of which have been missed by previous infrared or radio continuum studies. Systematic studies of other massive clouds in the CMZ, using high resolution, sensitive maser and submillimeter observations, will be helpful to establish their star formation status. One such example is the SMA Legacy Survey of the CMZ[11] (PIs: C. Battersby & E. Keto) that will cover all regions in the CMZ above a column density threshold of 10^{23} cm^{-2} using the same setups as our SMA observations.

A virial analysis shows that among the 17 dense cores traced by dust emission, 12 cores are gravitationally bound. The 13 H_2O masers associated with the dense cores likely trace protostellar outflows. The star formation in the 20 $km\,s^{-1}$ cloud appears to be in an early evolutionary phase, before significant heating or ionization of ambient gas. This cloud may follow the tidal compression and triggered collapse model of Longmore et al. (2013b) and Kruijssen et al. (2015), similar to the dust ridge clouds. However, its star formation rate is higher than in G0.253+0.016, which likely reflects local differences in initial conditions.

We thank the anonymous referee for constructive comments, and Elisabeth Mills and Hauyu Baobab Liu for helpful discussion. X.L. acknowledges the support of a Smithsonian Predoctoral Fellowship and the program A for outstanding PhD candidate of Nanjing University. T.P. acknowledges financial support from the *Deutsche Forschungsgemeinschaft, DFG* via the SPP (priority program) 1573 ("Physics of the ISM"). J.M.D.K. is funded by a Gliese Fellowship. This work is supported by the SI CGPS grant on Star Formation in the Central Molecular Zone of the Milky Way, the National Natural Science Foundation of China (grants 11328301, 11273015 and 11133001), and the National Basic Research Program (973 program No. 2013CB834905).

REFERENCES

Bally, J., Aguirre, J., Battersby, C., et al. 2010, ApJ, 721, 137

Battersby, C., Bally, J., Jackson, J. M., et al. 2010, ApJ, 721, 222

Bertoldi, F., & McKee, C. F. 1992, ApJ, 395, 140

Beuther, H., Schilke, P., Menten, K. M., et al. 2005, ApJ, 633, 535

Breen, S. L., Caswell, J. L., Ellingsen, S. P., & Phillips, C. J. 2010, MNRAS, 406, 1487

Breen, S. L., Ellingsen, S. P., Caswell, J. L., et al. 2014, MNRAS, 438, 3368

[11] https://www.cfa.harvard.edu/sma/largeScale/CMZ/

Caswell, J. L., Breen, S. L., & Ellingsen, S. P. 2011, MNRAS, 410, 1283

Caswell, J. L., Fuller, G. A., Green, J. A., et al. 2010, MNRAS, 404, 1029

Downes, D., Goss, W. M., Schwarz, U. J., & Wouterloot, J. G. A. 1979, A&AS, 35, 1

Ekers, R. D., van Gorkom, J. H., Schwarz, U. J., & Goss, W. M. 1983, A&A, 122, 143

Elitzur, M., Hollenbach, D. J., & McKee, C. F. 1989, ApJ, 346, 983

Fontani, F., Cesaroni, R., & Furuya, R. S. 2010, A&A, 517, A56

Furuya, R. S., Kitamura, Y., Wootten, H. A., Claussen, M. J., & Kawabe, R. 2001, ApJ, 559, L143

Goldsmith, P. F., Lis, D. C., Hills, R., & Lasenby, J. 1990, ApJ, 350, 186

Johnston, K. G., Beuther, H., Linz, H., et al. 2014, A&A, 568, A56

Kauffmann, J., Pillai, T., & Goldsmith, P. F. 2013a, ApJ, 779, 185

Kauffmann, J., Pillai, T., & Zhang, Q. 2013b, ApJ, 765, L35

Kendrew, S., Ginsburg, A., Johnston, K., et al. 2013, ApJ, 775, L50

Kruijssen, J. M. D., Dale, J. E., & Longmore, S. N. 2015, MNRAS, 447, 1059

Kruijssen, J. M. D., Longmore, S. N., Elmegreen, B. G., et al. 2014, MNRAS, 440, 3370

Krumholz, M. R., & Kruijssen, J. M. D. 2015, MNRAS, 453, 739

Lindqvist, M., Winnberg, A., Habing, H. J., & Matthews, H. E. 1992, A&AS, 92, 43

Lis, D. C., Menten, K. M., Serabyn, E., & Zylka, R. 1994, ApJ, 423, L39

Longmore, S. N., Rathborne, J., Bastian, N., et al. 2012, ApJ, 746, 117

Longmore, S. N., Kruijssen, J. M. D., Bally, J., et al. 2013a, MNRAS, 433, L15

Longmore, S. N., Bally, J., Testi, L., et al. 2013b, MNRAS, 429, 987

McMullin, J. P., Waters, B., Schiebel, D., Young, W., & Golap, K. 2007, in Astronomical Society of the Pacific Conference Series, Vol. 376, Astronomical Data Analysis Software and Systems XVI, ed. R. A. Shaw, F. Hill, & D. J. Bell, 127

Menten, K. 1991, in Astronomical Society of the Pacific Conference Series, Vol. 16, Atoms, Ions and Molecules: New Results in Spectral Line Astrophysics, ed. A. D. Haschick & P. T. P. Ho (San Francisco: ASP), 119

Mezger, P. G., & Henderson, A. P. 1967, ApJ, 147, 471

Mills, E. A. C., Butterfield, N., Ludovici, D. A., et al. 2015, ApJ, 805, 72

Mottram, J. C., Hoare, M. G., Davies, B., et al. 2011, ApJ, 730, L33

Palla, F., Cesaroni, R., Brand, J., et al. 1993, A&A, 280, 599

Pillai, T., Kauffmann, J., Tan, J. C., et al. 2015, ApJ, 799, 74

Qin, S.-L., Zhao, J.-H., Moran, J. M., et al. 2008, ApJ, 677, 353

Rathborne, J. M., Longmore, S. N., Jackson, J. M., et al. 2015, ApJ, 802, 125

Reid, M. J., Menten, K. M., Zheng, X. W., et al. 2009, ApJ, 700, 137

Sault, R. J., Teuben, P. J., & Wright, M. C. H. 1995, in Astronomical Society of the Pacific Conference Series, Vol. 77, Astronomical Data Analysis Software and Systems IV, ed. R. A. Shaw, H. E. Payne, & J. J. E. Hayes, 433

Sevenster, M. N., Chapman, J. M., Habing, H. J., Killeen, N. E. B., & Lindqvist, M. 1997, A&AS, 122, 79

Sjouwerman, L. O., Lindqvist, M., van Langevelde, H. J., & Diamond, P. J. 2002, A&A, 391, 967

Sjouwerman, L. O., & van Langevelde, H. J. 1996, ApJ, 461, L41

Sjouwerman, L. O., van Langevelde, H. J., Winnberg, A., & Habing, H. J. 1998, A&AS, 128, 35

Szymczak, M., Pillai, T., & Menten, K. M. 2005, A&A, 434, 613

Tarter, T. C., & Welch, W. J. 1986, ApJ, 305, 467

Titmarsh, A. M., Ellingsen, S. P., Breen, S. L., Caswell, J. L., & Voronkov, M. A. 2014, MNRAS, 443, 2923

Urquhart, J. S., Moore, T. J. T., Menten, K. M., et al. 2015, MNRAS, 446, 3461

Walsh, A. J., Breen, S. L., Britton, T., et al. 2011, MNRAS, 416, 1764

Yusef-Zadeh, F., Cotton, W., Viti, S., Wardle, M., & Royster, M. 2013, ApJ, 764, L19

Yusef-Zadeh, F., Lacy, J. H., Wardle, M., et al. 2010, ApJ, 725, 1429

Yusef-Zadeh, F., Hewitt, J. W., Arendt, R. G., et al. 2009, ApJ, 702, 178

Table 1. Summary of the observations.

Telescope	PI	Project ID	Lines	Date	$\tau_{225\ \mathrm{GHz}}$	T_{sys} (K)	Pointing[a]	Calibrators			Note
								Bandpass	Flux	Gain[b]	
SMA Compact	X. Lu	2013A-S049	Many	2013 Jul 24	0.25	100–400	S1–S8	3C84	Neptune	Q1, Q2	6 antennas
				2013 Aug 03	0.10	100–240	S1–S8	3C84	Neptune	Q1, Q2	5 antennas
				2013 Aug 09	0.20	100–240	S1–S8	1924−292	Neptune	Q1, Q2	5 antennas
SMA Subcompact	Q. Zhang	2012B-S097	Many	2013 May 21	0.17	120–180	S1–S8	3C279	Neptune, Titan	Q1, Q2	5 antennas
VLA DnC	Q. Zhang	13A-307	NH_3 (1,1)–(5,5), H_2O maser, 1.3 cm continuum	2013 May 12	···	···	V1–V3	3C279	3C286	Q2	···

[a]Coordinates of pointing centers: S1: (17:45:38.35, −29:03:49.90); S2: (17:45:38.77, −29:04:18.60); S3: (17:45:38.64, −29:04:46.20); S4: (17:45:38.10, −29:05:13.90); S5: (17:45:37.55, −29:05:40.40); S6: (17:45:36.80, −29:06:07.60); S7: (17:45:35.00, −29:06:19.10); S8: (17:45:36.79, −29:06:31.10); V1: (17:45:38.60, −29:04:09.50); V2: (17:45:38.00, −29:05:08.80); V3: (17:45:36.60, −29:06:05.00).

[b]Gain calibrators: Q1: 1733−130; Q2: 1744−312.

Table 2. Properties of the dense cores.

Core ID	R.A. & Decl. (J2000)	Maj. × Min.[a] ($''\times''$)	PA[a] (°)	Flux[b] (mJy)	FWHM[c] ($\mathrm{km\,s^{-1}}$)	$M_{\rm core}$ ($M_\odot$)	α
C1-P1	17:45:37.58, -29:03:48.83	7.22 × 3.16	48.8	648.1	3.0 (N)	1309	0.17
C1-P2	17:45:38.18, -29:03:40.31	11.1 × 2.75	28.4	191.7	2.9 (N)	387	0.62
C1-P3	17:45:39.17, -29:03:41.03	12.2 × 3.32	5.25	112.7	4.2 (N)	228	2.32
C2-P1	17:45:38.23, -29:04:26.60	10.1 × 4.10	36.0	189.0	5.8 (N)	382	2.55
C2-P2	17:45:38.62, -29:04:18.69	9.10 × 5.02	22.7	118.5	3.2 (N)	239	1.45
C2-P3	17:45:39.04, -29:04:13.24	6.98 × 3.96	34.7	87.8	2.5 (N)	177	1.02
C3-P1	17:45:37.81, -29:05:02.41	6.38 × 3.12	178.0	208.1	4.3 (H)	420	0.92
C3-P2	17:45:37.62, -29:05:16.65	8.99 × 0.49	3.1	63.0	···	127	···
C3-P3	17:45:38.28, -29:04:58.59	8.96 × 5.11	90.8	112.7	···	228	···
C4-P1	17:45:37.64, -29:05:43.65	7.85 × 5.35	68.0	935.4	3.6 (N)	1889	0.22
C4-P2	17:45:38.23, -29:05:32.72	14.0 × 3.51	30.5	393.2	3.6 (C)	794	0.56
C4-P3	17:45:35.36, -29:05:55.53	4.07 × 1.70	99.0	104.1	3.8 (C)	210	0.87
C4-P4	17:45:36.25, -29:05:49.03	5.00 × 2.70	56.0	76.4	5.0 (N)	154	2.73
C4-P5	17:45:36.74, -29:05:45.93	<5.23 × <3.07	···	35.3	2.4 (N)	71	1.82
C4-P6	17:45:37.16, -29:05:55.13	3.41 × 2.63	6.2	37.9	2.3 (C)	76	1.19
C5-P1	17:45:36.71, -29:06:17.50	7.12 × 3.93	73.4	189.7	2.7 (N)	383	0.54
C5-P2	17:45:36.43, -29:06:19.55	6.57 × 4.45	13.1	151.2	2.3 (N)	305	0.54

[a]Major and minor FWHMs and position angles of the cores are deconvolved from the beam.

[b]Fluxes are corrected for primary-beam response.

[c]Letters in parentheses indicate the lines used to estimate FWHM: N - N_2H^+; C - $C^{18}O$; H - H_2CO.

Table 3. Properties of the H_2O masers.

Maser ID	R.A. & Decl. (J2000)	$v_{\rm peak}$[a] ($\rm km\,s^{-1}$)	$F_{\rm peak}$[a] (mJy)	$F_{\rm integrated}$[b] ($\rm mJy{\cdot}km\,s^{-1}$)	$L_{\rm H_2O}$ ($10^{-7}\ L_\odot$)	Dense Cores
W1	17:45:38.10, -29:03:41.75	14.8, 19.0	431, 100	430	7.0	C1-P2
W2	17:45:37.73, -29:03:46.29	21.5, 27.8	131, 161	775	12.6	C1-P1
W3	17:45:37.48, -29:03:49.15	24.5, 28.1	999, 1022	3797	61.8	C1-P1
W4	17:45:34.63, -29:04:36.42	2.4	396	670	10.9	···
W5	17:45:37.76, -29:05:01.91	-32.2, 18.6	180, 13180	6822	110.0	C3-P1
W6	17:45:40.75, -29:05:01.93	12.7	225	357	5.8	···
W7	17:45:35.85, -29:05:08.75	51.0	212	186	3.0	···
W8	17:45:37.68, -29:05:13.57	46.2	17	18	0.3	C3-P2
W9	17:45:37.52, -29:05:22.59	-40.8, -40.2	33, 35	46	0.7	···
W10	17:45:37.16, -29:05:41.70	-18.7, 10.8	54, 93	196	3.2	C4-P1
W11	17:45:37.62, -29:05:43.92	4.5, 9.9	783, 507	3258	53.0	C4-P1
W12	17:45:37.51, -29:05:43.89	13.1, 16.9	110, 99	264	4.3	C4-P1
W13	17:45:37.90, -29:05:44.24	-21.5, 26.4	23, 23	55	0.9	C4-P1
W14	17:45:36.72, -29:05:46.02	-25.5, -24.6	84, 171	246	4.0	C4-P5
W15	17:45:36.33, -29:05:49.52	5.5, 13.1	972, 1178	2377	38.7	C4-P4
W16	17:45:35.15, -29:05:53.62	-4.8, -4.4	26, 24	48	0.8	C4-P3
W17	17:45:37.11, -29:05:54.38	-3.8, -3.1	171, 159	302	4.9	C4-P6
W18	17:45:34.77, -29:06:02.43	20.3, 20.7	17, 16	33	0.5	···

[a]Peak fluxes are not corrected for primary-beam response. For masers with more than two velocity components, only the two strongest peaks are listed.

[a]Integrated fluxes are corrected for primary-beam response.

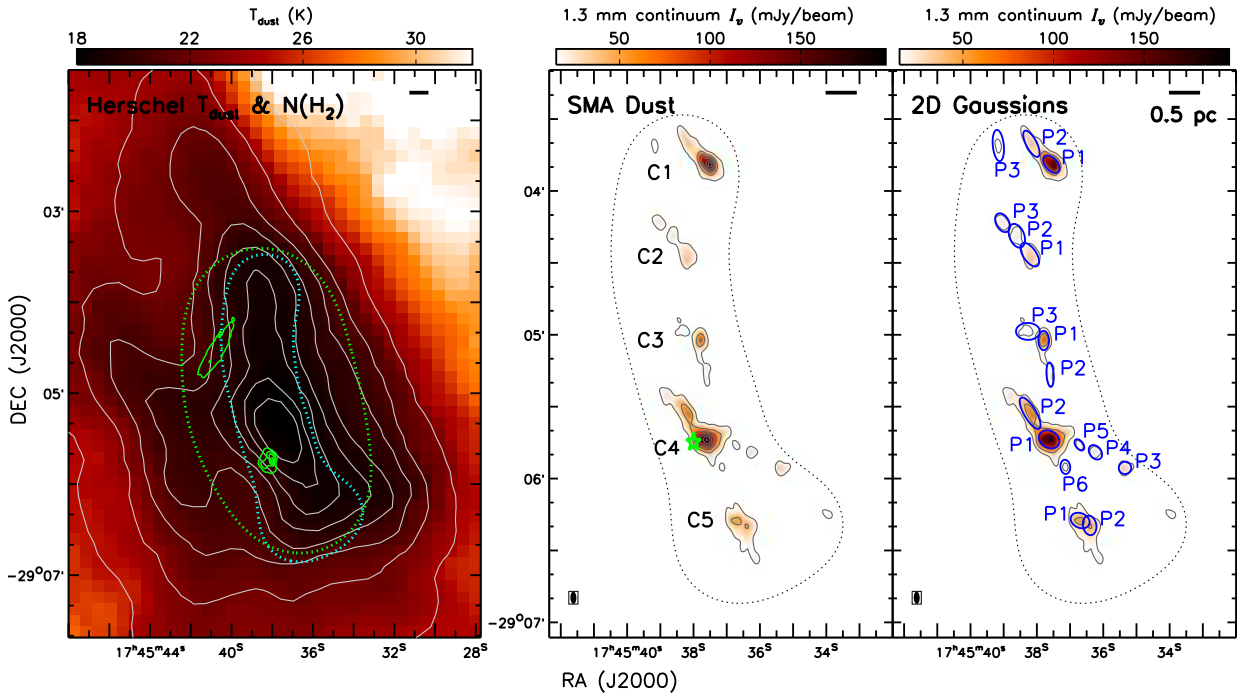

Fig. 1.— Left: Herschel dust temperature is shown in the background image. The white contours present the Herschel H_2 column density, between 5×10^{22} cm^{-2} and 4×10^{23} cm^{-2} in step of 5×10^{22} cm^{-2}. The green contours present the VLA 1.3 cm continuum emission, between 2 mJy beam^{-1} and 18 mJy beam^{-1} in step of 4 mJy beam^{-1}. The cyan and green dotted loops show the FHWMs of the SMA and VLA primary beam responses, respectively. Middle: both contours and background image show the SMA 1.3 mm continuum emission. The contours are between 5σ and 65σ levels in step of 10σ, where 1σ=3 mJy beam^{-1}. The five clumps are labeled. The dotted loop shows the FWHM of the SMA primary beam response. The synthesized beam of the SMA is shown in the lower left corner. The H II region is marked by a green star. Right: same as the middle panel, but only the 5σ and 15σ contours are plotted. The ellipses are the results of 2D Gaussian fittings.

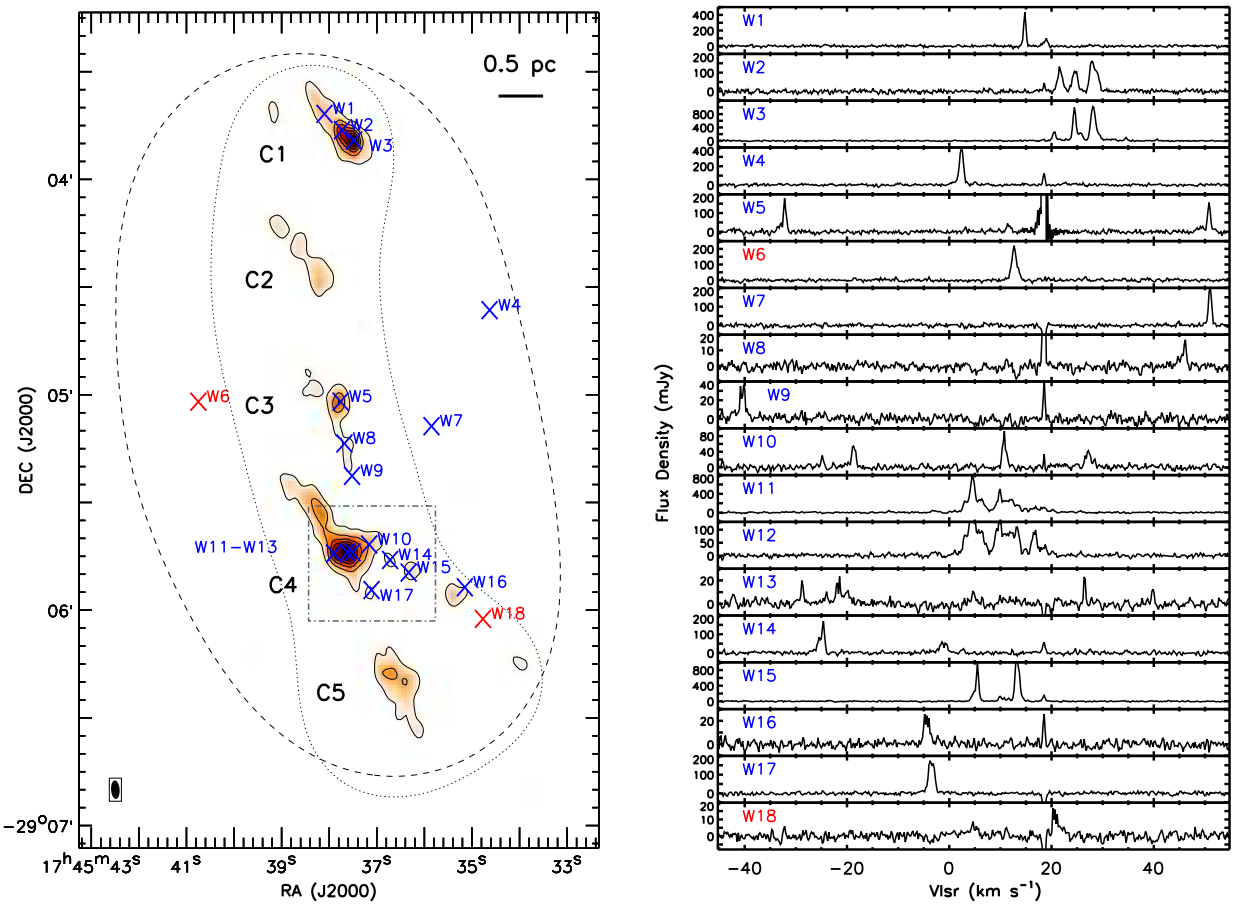

Fig. 2.— Left: the crosses show the H_2O masers. The two red crosses (W6, W18) are known OH/IR stars. The blue crosses show H_2O masers without known OH/IR star counterparts. Both the contours and the background image show the SMA 1.3 mm continuum emission. The loops are the same as in Figure 1. Right: the spectra of the 18 H_2O masers. The features at $\sim$18 km s^{-1}, either in emission or in absorption, are from sidelobes of the strongest maser, W5.